RESEARCH ARTICLE | NOVEMBER 16 2021

Strain engineering of quasi-1D layered TiS_3 nanosheets toward giant anisotropic Raman and piezoresistance responses

Special Collection: One-Dimensional van der Waals Materials

Jing-Kai Qin ; Hai-Lin Sun; Tong Su; Weiwei Zhao ; Liang Zhen ; Yang Chai ; Cheng-Yan Xu

Appl. Phys. Lett. 119, 201903 (2021)
https://doi.org/10.1063/5.0069569

Applied Physics Letters ARTICLE scitation.org/journal/apl

Strain engineering of quasi-1D layered TiS_3 nanosheets toward giant anisotropic Raman and piezoresistance responses

Cite as: Appl. Phys. Lett. **119**, 201903 (2021); doi: 10.1063/5.0069569
Submitted: 31 August 2021 · Accepted: 1 November 2021 ·
Published Online: 16 November 2021

Jing-Kai Qin,[1] Hai-Lin Sun,[1] Tong Su,[1] Weiwei Zhao,[1] Liang Zhen,[1,2] Yang Chai,[3,a)] and Cheng-Yan Xu[1,2,a)]

AFFILIATIONS

[1]Sauvage Laboratory for Smart Materials, School of Materials Science and Engineering, Harbin Institute of Technology (Shenzhen), Shenzhen 518055, China
[2] MOE Key Laboratory of Micro-Systems and Micro-Structures Manufacturing, Harbin Institute of Technology, Harbin 150080, China
[3]Department of Applied Physics, The Hong Kong Polytechnic University, Kowloon, Hong Kong 999077, China

Note: This paper is part of the APL Special Collection on One-Dimensional van der Waals Materials.
[a)]**Authors to whom correspondence should be addressed:** ychai@polyu.edu.hk and cy_xu@hit.edu.cn

ABSTRACT

Quasi-one-dimensional layered TiS_3 nanosheets possess highly anisotropic physical properties. Herein, we reported the anisotropic strain response of Raman and the piezoresistance effect in layered TiS_3 nanosheets. An attractive Grüneisen parameter (γ_m) of 5.82 was achieved for A_g^{III} mode in the *b*-axis strained TiS_3 nanosheet, while a negligible value of γ_m was obtained when the strain is applied along the *a*-axis direction. We also revealed the opposite piezoresistive effect with strains applied along the two principal axes, demonstrating a gauge factor ratio of approximately −1:3.2. The giant anisotropy is attributed to the strain modulated bandgap, which was further confirmed by density functional theory calculations.

Strain engineering has proven to be an effective way to manipulate the physical properties of atomically thin two-dimensional (2D) materials.[1,2] The unique mechanical properties of 2D materials allow the presence of a large degree of strain before fracture. The strong coupling effect of strain to electronic structures enables a broad tunability of their physical properties and the implement of functional electronic devices.[1–7] For example, Zhang *et al.* employed strain engineering to alter the electrical properties of black phosphorus (B-P), a typical 2D material with a direct bandgap of 0.33 eV.[8] The continuous bandgap modulation under strain would induce the density change of thermally activated carriers and leads to a remarkable piezoresistive effect in B-P field-effect transistors (FETs).

Semiconducting materials with a low-symmetry crystal structure exhibit strong in-plane anisotropy of physical properties, which imbue more freedom for designing electronic devices with novel functionalities.[9–11] Particularly, titanium trisulfide (TiS_3) crystallizes in the monoclinic *P21/m* space group.[12] As illustrated in Fig. 1(a), the Ti atoms at the center are bonded with neighboring S atoms into triangular distorted prisms, which are further connected along the *b*-axis into atomic chains. These repeating parallel chains are covalently bonded within the *a*-*b* plane into the monolayer structure while weakly stacked via vdW interaction along the *c*-axis, resulting into a quasi-1D layered structure. The reduced symmetry of the crystal structure gives rise to the high anisotropy in its electronic and optical characteristics[13–21] and offers unexplored possibilities for the modulation of physical properties via strain-engineering.[22–24]

In this work, we studied the anisotropic strain response of lattice vibration and piezoresistive effect in TiS_3 nanosheets. As tensile strain is applied along *b*-axis, the A_g^{III} Raman mode of TiS_3 shift approximately 14 $cm^{-1}\%^{-1}$, while it exhibits nearly zero response when applied with strain along the *a*-axis direction. TiS_3 nanosheets exhibit positive and negative piezoresistance along the *a*- and *b*-axes, respectively. These results demonstrate that the strain engineering is highly efficient to modulate the optical and electrical properties of quasi-1D layered TiS_3. The giant anisotropic response is critical to understand the unique structure–property relationship in quasi-1D TiS_3 nanosheets and develop future electronic devices with multi-functionalities.

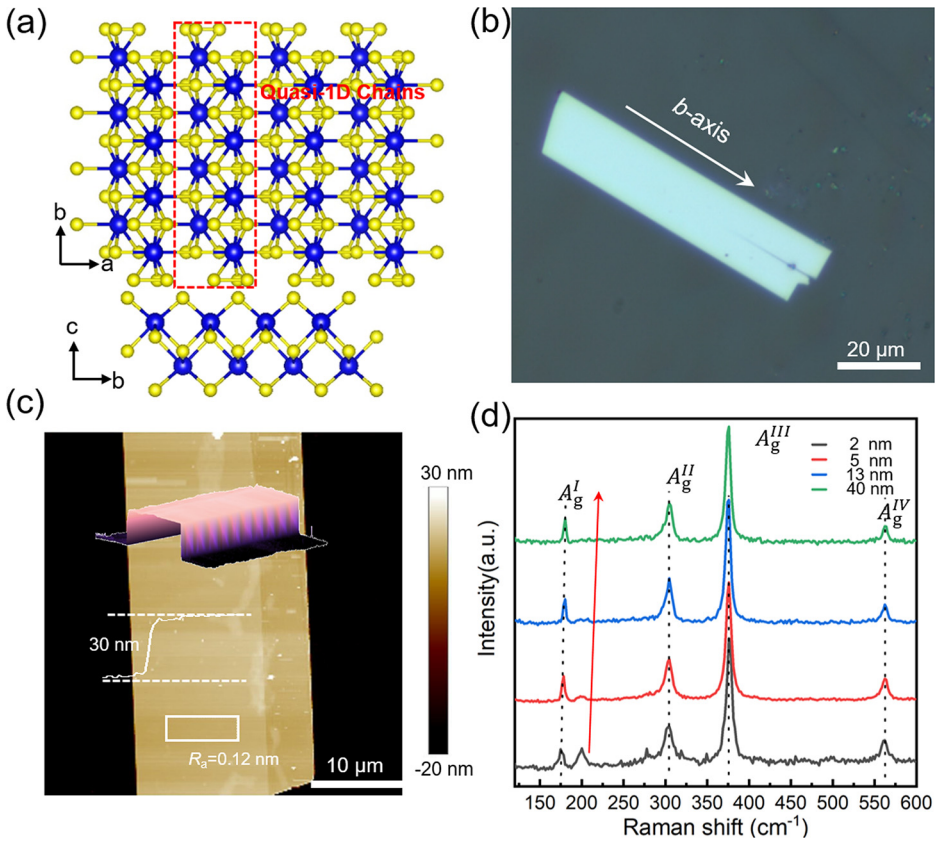

FIG. 1. Materials characterization of quais-1D TiS_3 nanosheets. (a) Crystal structure of monolayer TiS_3. The quasi-1D chains are formed by connecting triangular prisms along the *b*-axis direction. (b) and (c) OM and AFM images of a 30 nm-thick TiS_3 nanosheet on the SiO_2/Si substrate. Inset image in (c) shows the corresponding 3D view. (d) Raman spectra of TiS_3 nanosheets with different thicknesses. The data were collected from fresh samples grown on the mica substrate. Peak locating at ~200 cm^{-1} is from the mica substrate.

TiS_3 nanosheets were obtained through a facile chemical vapor transport (CVT) process by direct reaction of titanium and sulfur in a sealed ampule at 550 °C. A microreactor constructed by vertically stacked mica is located at the end of ampule in which the space confinement effect enables the in-plane growth of TiS_3. After 72 h of growth, the resulting TiS_3 nanosheets on mica substrate were characterized by optical microscopy (OM) and atomic force microscopy (AFM). Although the thickness of TiS_3 can be scaled down to a 2 nm limit, most of them have a small lateral size (less than 3 μm) that is not large enough for device fabrication (Fig. S1 in the supplementary material). Therefore, samples with thickness ranging from 20 to 50 nm were employed for Raman spectroscopy and electrical measurement. Figures 1(b) and 1(c) show a typical OM image of the 30 nm-thick TiS_3 sample and corresponding AFM image. We can see that the rectangular TiS_3 nanosheet has an atomically flat surface with a roughness (R_a) of less than 0.12 nm.

Raman spectroscopy was employed to study the vibrational properties of TiS_3 nanosheets. As shown in Fig. 2(a), five Raman active modes located at 176, 298, 370, 402, and 556 cm^{-1} can be clearly resolved. The frequency peak at 176 cm^{-1} is labeled as A_g^I, which involves the out-of-plane vibration of quasi-1D atomic chains of TiS_3[12]. Therefore, the peak position of A_g^I mode is highly dependent on the layer number of TiS_3 nanosheet, which can blue-shift by as large as 5 cm^{-1} with the thickness increasing from 2 to 45 nm [Figs. 1(d) and S2 in the supplementary material]. Both of the peaks at 298 cm^{-1} (A_g^{II}) and 370 cm^{-1} (A_g^{III}) are originated from the displacement of TiS_3 atoms within the in-plane layer. The A_g^{II} mode represents that two degenerated optical branches coincide with each other in which the difference lies in the relative vibration direction between the Ti and S atoms across the two individual Ti-S prisms. The A_g^{III} mode relates to the opposite vibration of Ti and S atoms in a single prism, whereas the vibration of atoms in the neighboring prism is in a centrosymmetric way. For the A_g^{IV} mode, it is predominantly composed of the in-plane motion of S–S pair and part of out-of-plane vibration of Ti-S bonding. It was shown that a small peak at 402 cm^{-1} is also revealed, which belongs to the B_g^{III} vibrational mode. The peak shows an extremely weak intensity, and it would cause immense hardship for data processing. Therefore, we only focus on the four main vibration modes locating at 176, 298, 370, and 556 cm^{-1}.

To investigate the anisotropic lattice vibration of TiS_3 nanosheet, angle-resolved Raman spectra were collected by rotating the sample with a step of 15°. The peak intensity of Raman-active modes is quite sensitive to the polarized angle (Fig. S3 in the supplementary material), and corresponding polar figures can be generated and plotted as shown in Fig. 2(b). TiS_3 nanosheet was initially aligned with the *b*-axis parallel to the polarized direction of the incident laser, and the angle in this configuration is defined as 0°. The polar plot of A_g^{III} mode is in the form of a horizonal two-lobed shape, and the intensity of peak reaches the max/min values when the lasers are polarized along the *b*/*a*-axes directions of TiS_3 nanosheets. The aspect ratio of peak intensity (r = max/min) was calculated to be 4.28 for the A_g^{III} mode. It should be noted that the two lobes shown in the polar figures are rotated by

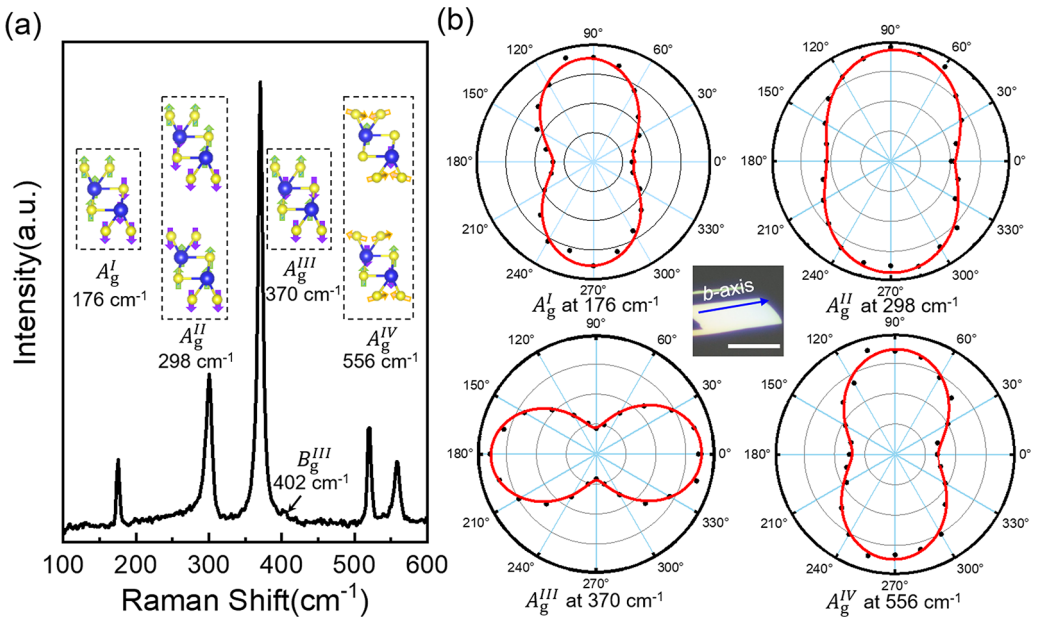

FIG. 2. Angle-dependent Raman spectra of TiS_3 nanosheets transferred onto the Si/SiO_2 substrate. (a) Typical Raman spectrum of TiS_3 nanosheet measured at room temperature. Inset legends illustrate the corresponding atomic motion of different branches. The peak locating at 521 cm^{-1} is from the SiO_2/Si substrate. (b) Polar plots of different vibration modes at 176, 298, 370, and 556 cm^{-1}. The inset image shows a TiS_3 nanosheet with the *b*-axis parallel with the polarized direction of the incident laser. Scale bar is 10 μm.

90° for the A_g^I, A_g^{II}, and A_g^{IV} modes, with the aspect ratios of 2.61, 1.71, and 2.50, respectively. The peak intensity of B_g^{III} mode exhibits weak anisotropy, and the aspect ratio was calculated to be 1.14 (Fig. S4 in the supplementary material).

The anisotropic lattice vibrational properties of TiS_3 nanosheets are well in consistent with previous reports,[25] which can be explained by the subtle variations in the atomic spacing and bond lengths of TiS_3. The remarkable anisotropy of lattice vibration provides a nondestructive and feasible approach for the determination of the crystallographic direction.

Based on our experiment setup, uniaxial strain was applied along the *b*- and *a*- axes of TiS_3 nanosheet to evaluate the strain response of lattice vibration. Tensile strain (ε) was estimated using formula: $\varepsilon = d/2r$, where d and r are the thickness and radius of curvature of the flexible PET substrate. Polymethyl methacrylate (PMMA) with a thickness of 100 nm was spin-coated on TiS_3 nanosheet to prevent the slippage during strain loading [Fig. 3(a)]. The PET substrate with a thickness of 120 μm was initially bended along the *b*-axis direction of TiS_3 nanosheets. In other words, tensile strain is applied parallelly with the direction of quais-1D TiS_3 atomic chains. As shown in Fig. 3(b), all the A_g^I, A_g^{II}, and A_g^{III} modes experience an apparent red-shift of frequency, while the A_g^{IV} mode almost exhibits zero-response even with a large strain of 0.85%.

The change in the Raman shift rate of different vibration modes can be well explained by the change in atomic bonding characteristics under strain. Tensile strain along the *b*-axes causes the elongation of the Ti−S covalent bond length, which would weaken the interatomic interactions and lead to the reduction in vibration frequency. As the mapping plot shown in Fig. 3(c), the A_g^{III} mode locating at 370 cm^{-1} is the most sensitive to the tensile strain, and the Raman shift rate up to 14 cm^{-1}%$^{-1}$ can be achieved. Such a value is the highest value among the previously reported 2D nanosheets (e.g., B-P,[5] MoS_2,[26] tellurene,[27] and selenene[28]) and 1D materials (e.g., ZnO[29] and Ge[30]). The PMMA coating plays an important role for the strain-engineering of TiS_3 nanosheet. The Raman shift rate of A_g^{III} mode is only 4 cm^{-1}%$^{-1}$ without the PMMA encapsulation (Fig. S5 in the supplementary material). Similarly, tensile strain along the *b*-axis direction would also influence the relative vibration between the Ti atoms, bridge S atoms, and S–S pairs across the two prisms, resulting into the red-shift of the A_g^{II} mode with a shift rate of 6 cm^{-1}%$^{-1}$. The A_g^I mode mainly involves the relative motion of individual quasi-1D TiS_3 chains, which is hardly affected by the *b*-axis tensile strain; thus, minor shift of Raman frequency was observed with a small value of 2 cm^{-1}%$^{-1}$. For the zero-response of A_g^{IV} mode, we can ascribe it to the fact that it mainly involves the relative motion of S–S pairs perpendicular to the direction of TiS_3 chains, which is insensitivity to *b*-axis deformation.

Grüneisen parameter (γ_m) represents the shift rate of the vibration mode as lattice expanding,[31] and it can be calculated by applying formular:

$$\gamma_m = -\frac{1}{\omega_m}\frac{\Delta\omega_m}{\Delta\varepsilon}, \quad (1)$$

where ω_m represents the Raman frequencies at the zero strain. The uniaxial strain ε can be expressed as $\varepsilon = \varepsilon_b + \varepsilon_a = \varepsilon_b - \upsilon\varepsilon_b$, where υ is the Poisson's ratio. Since TiS_3 nanosheet locates on a PET substate with PMMA film coating, γ_m can be calculated according to Eq. (1) with the Poisson's ratio of $\upsilon = 0.33$ for PET.[32] The maximum value of 5.82 was obtained for A_g^{III} mode, which is about 1.5 times higher than

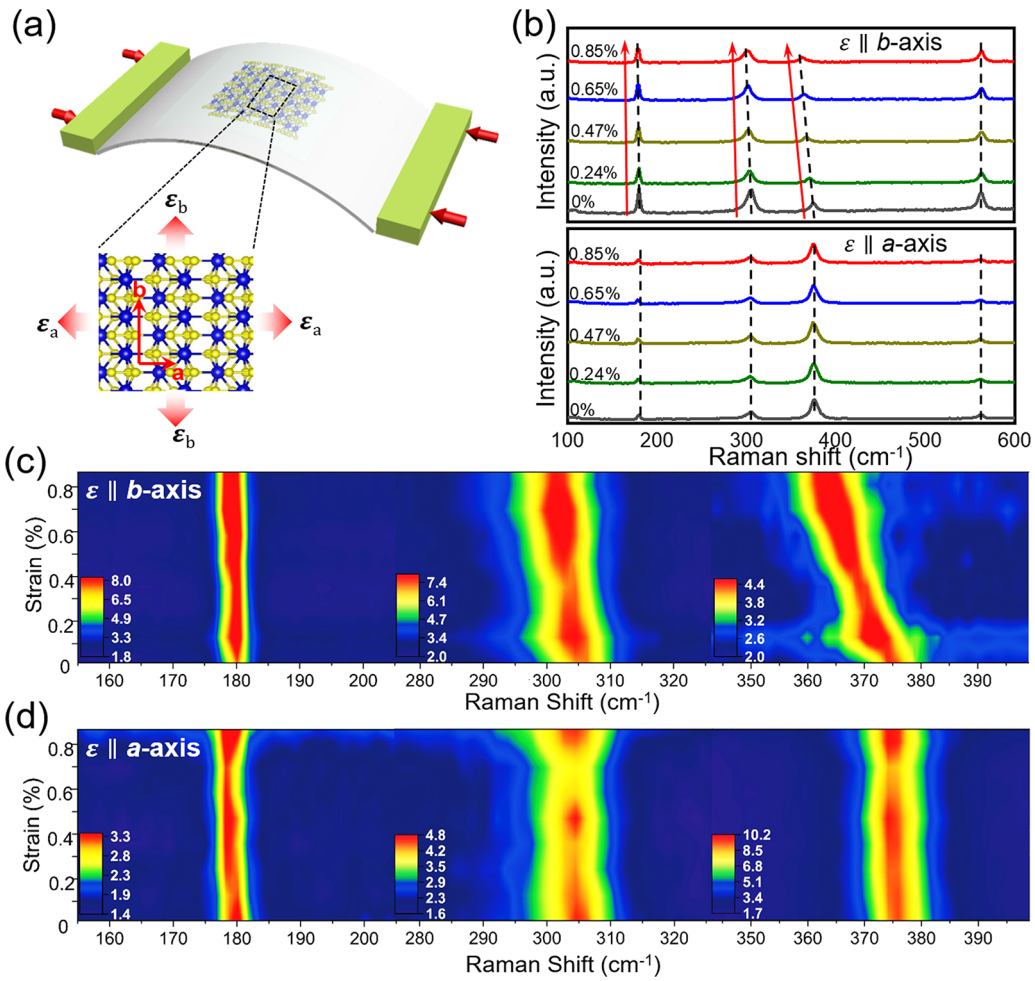

FIG. 3. Anisotropic strain response of lattice vibrational properties of TiS_3 nanosheets. (a) Schematic diagram of the experimental setup. The applying of anisotropic tensile strain is realized using a two-point bend approach. (b) Raman spectrum evolution of TiS_3 nanosheet with the tensile strain applied along the *b*-axis and *a*-axis directions, respectively. (c) Mapping plots of different vibration modes at 176, 298, 370, and 556 cm^{-1} in *b*-axis strained TiS_3. (d) Corresponding mapping plots in *a*-axis strained TiS_3.

the value of B-P ($\gamma_{B_{2g}} = 3.69$)[5], and even an order of magnitude higher than that of isotropic MoS_2 ($\gamma_{E^1_{2g}} = 0.6$)[32]. The results provide a pronounce evidence of the extraordinary anharmonic effect and strong interaction of atoms along quasi-1D TiS_3 chains.

We note that the strain response of lattice vibration along *a*-axis is quite different from that along the *b*-axis direction. Strain mapping was plotted by extracting the data from the Raman spectra [Fig. 3(d)]. Even with a large strain of 0.85%, TiS_3 nanosheet does not show significant photon frequency shift, and γ_m along *a*-axis is almost negligible. The negligible strain response is highly associated with the weak interactions between quasi-1D TiS_3 chains. Figure S6 in the supplementary material summarizes the frequency shift of strained TiS_3 nanosheet along these two directions. The strain-engineered giant anisotropy of lattice vibration conclusively verified the anisotropic nature of TiS_3 crystals.

Strain engineering also enables efficient control of the physical properties of 2D semiconducting material,[32–34] thus providing many opportunities for advanced mechanical-electronic device applications. To investigate the anisotropic strain response of electrical conductance in quasi-1D layered TiS_3, two-terminal devices with *a*/*b*-axes channels were fabricated based on the TiS_3 nanosheet on the PET substate. To ensure a reliable electrical contact during measurement, Au/Ti (50/5 nm) metal electrodes are patterned with a large width of 200 μm, and the channel length is set to be 10 μm. Figure 4(a) plots the real-time resistance change in the *b*-axis channel device as the strain is applied along the *b*-axis direction. It demonstrates a stable and repeated strain modulation of resistance under strain between 0% and 0.85%. The metric of the gauge factor (*GF*) of piezoresistance is used to evaluate the piezoresistive sensitivity, and it can be given as

$$GF = (\Delta R/R)/\varepsilon, \tag{2}$$

where R represents the resistance of the unstrained TiS_3 channel and ΔR is the resistance change under strain ε. *GF* along *b*-axis of TiS_3 nanosheet is calculated to be as high as ~224.7, which is much larger than that of previously reported multilayer MoS_2 (~50),[35] BP (~125),[8] and ReS_2 (~60.49).[2] The piezoresistance response of the

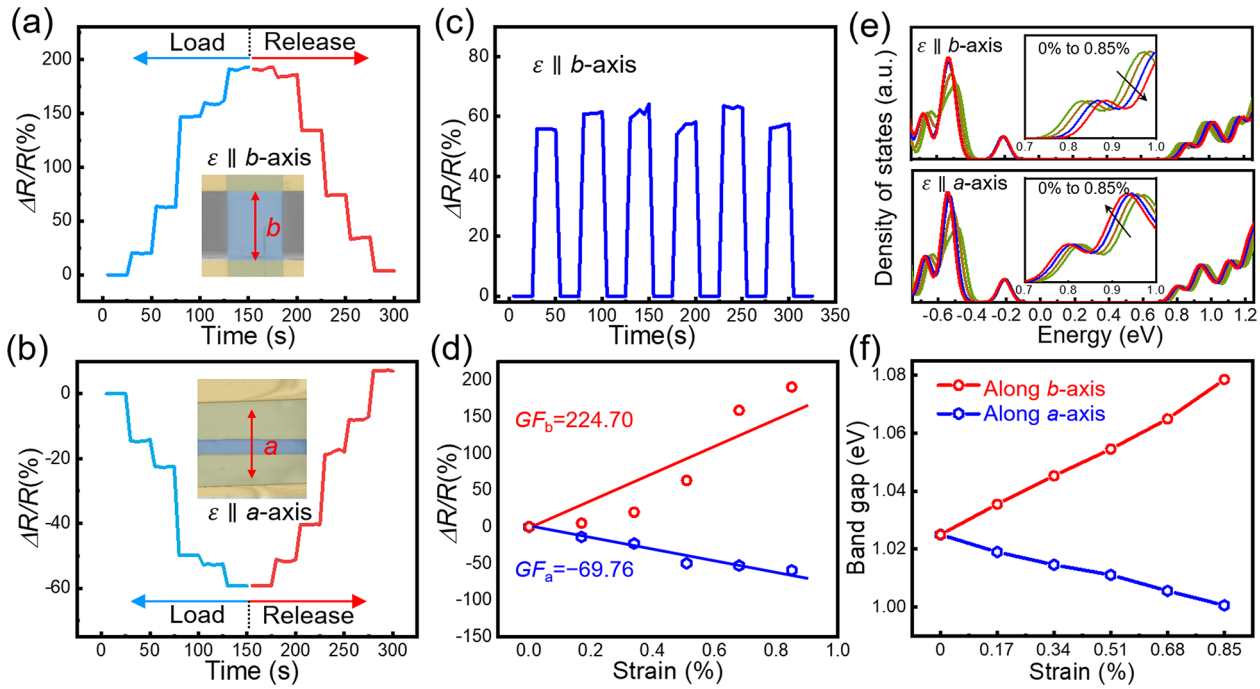

FIG. 4. Anisotropic piezoresistance effect in TiS_3 nanosheets. (a) and (b) Real-time measurement the resistance changes of *b*-axis and *a*-axis TiS_3 devices. Tensile strain is applied along the channel direction. Inset images shows the optical microscopy images of devices. (c) Repeatability of the piezo-resistance response of TiS_3 nanosheet with the channel patterned along the *b*-axis direction. (d) Relative resistance changes as a function of strain. (e) Theocratically calculated total energy states of *b*-axis and *a*-axis strained TiS_3 single crystals. (f) Variation of bandgap as a function of ε_a and ε_b.

device can be well repeated without degeneration even after five bending cycles, suggesting that TiS_3 nanosheet was deformed in the elastic regime [Fig. 4(c)].

The resistance drops slowly as the strain is applied along the *a*-axis direction [Fig. 4(b)], indicating the opposite piezoresistance compared to the *b*-axis strain. Figure 4(d) illustrates the relative resistance change in TiS_3 devices along these two orthogonal directions, both of which exhibit great linearity as a function of tensile strains. The *GFs* of TiS_3 nanosheet along the *a*- and *b*-axes are estimated to be −69.76 and 224.70, respectively, with a factor ratio of approximately −1:3.2.

The distinct anisotropy in piezoresistive properties of TiS_3 is associated with the strain-engineered bandgap structure.[2,4,23] The conductivity of semiconductors under tensile strain can be given as[35]

$$\sigma = \sigma_0 \exp\left[-\frac{\varepsilon}{2k_B T}\frac{\partial E_g}{\partial \varepsilon}\right], \tag{3}$$

where σ and σ_0 are the electrical conductance of strained and initial TiS_3 nanosheet, respectively. ε, k_B, and T represent the strain, Boltzmann constant, and temperature. $(\partial E_g)/\partial\varepsilon$ is the change rate of bandgap under tensile strain. We performed density functional theory (DFT) calculation to identify the energy band structure of strained TiS_3 (see a detailed simulation process in the supplementary material). A bandgap value of 1.025 eV was obtained for the unstrained TiS_3 nanosheets, and the direct bandgap structure can be well maintained with applied tensile strains (Fig. S7 in the supplementary material). Under 0.85% *b*-axis tensile strain, the bandgap would be broadened by 57 meV, reaching up to 1.082 eV. We also observed abnormal decrease in bandgap by about 25 meV as the tensile strain is applied along the *a*-axis direction [Figs. 4(e) and 4(f)]. According to Eq. (3), the opposite transition in the energy band structure would cause the increase/decrease in conductivity as the strains are applied along the *a*/*b* axes direction, which well explains the anisotropic piezoresistive effect in the TiS_3 nanosheet. The results indicate the promising applications of quasi-1D layered TiS_3 for developing piezo-functional devices with capability of detecting directional strains.

In conclusion, we demonstrated the anisotropic Raman response and piezoresistance in strained TiS_3 nanosheet. A high strain sensitivity with γ_m of 5.82 was demonstrated for the A_g^{III} mode in *b*-axis strained TiS_3, together with the near zero response in the *a*-axis strain samples. We also found that the resistance of TiS_3 nanosheet exhibits remarkable opposite strain response, showing positive and negative piezoresistance as the strain is applied along the *a*- and *b*-axes, respectively. The giant anisotropy of the piezoresistive effect can be explained well by the opposite bandgap transition along the two axes in strained TiS_3 nanosheet, which was confirmed by the DFT calculation. The distinct anisotropic characteristics make TiS_3 a versatile 2D semiconductor for designing novel electronic devices.

See the supplementary material for the detailed DFT simulation process, characterization of TiS_3 nanosheet with different thickness, the layer-dependent Raman spectra, the anisotropic frequency shift of TiS_3 nanosheet under *a*/*b*-axes strains, and the calculated band structure of strained TiS_3 nanosheets.

This work was supported by National Natural Science Foundation of China (Nos. 52102161 and 52073075), Shenzhen Training Programme Foundation for the Innovative Talents (No. RCBS20200714114911270), Shenzhen Science and Technology Program (Nos. KQTD20200820113045083, KQTD20170809110344233, and JCYJ20180507183424383), Natural Science Foundation of Guangdong Province (No. 2021A1515012423), and the Research Grant Council of Hong Kong (15205318).

AUTHOR DECLARATIONS

Conflict of Interest

The authors have no conflicts to disclose.

DATA AVAILABILITY

The data that support the findings of this study are available from the corresponding authors upon reasonable request.

REFERENCES

[1]Y. Wang, S. Yao, P. Liao, S. Jin, Q. Wang, M. J. Kim, G. J. Cheng, and W. Wu, Adv. Mater. **32**(29), 2002342 (2020).
[2]C. An, Z. Xu, W. Shen, R. Zhang, Z. Sun, S. Tang, Y.-F. Xiao, D. Zhang, D. Sun, and X. Hu, ACS Nano **13**(3), 3310–3319 (2019).
[3]S. Deng, A. V. Sumant, and V. Berry, Nano Today **22**, 14–35 (2018).
[4]R. Fei and L. Yang, Nano Lett. **14**(5), 2884–2889 (2014).
[5]Y. Li, Z. Hu, S. Lin, S. K. Lai, W. Ji, and S. P. Lau, Adv. Funct. Mater. **27**(19), 1600986 (2017).
[6]K. Wang, T. Hu, F. Jia, G. Zhao, Y. Liu, I. V. Solovyev, A. P. Pyatakov, A. K. Zvezdin, and W. Ren, Appl. Phys. Lett. **114**(9), 092405 (2019).
[7]S. Hussain, R. Xu, K. Xu, L. Lei, L. Meng, Z. Zheng, S. Xing, J. Guo, H. Dong, and A. Liaqat, Appl. Phys. Lett. **117**(15), 153102 (2020).
[8]Z. Zhang, L. Li, J. Horng, N. Z. Wang, F. Yang, Y. Yu, Y. Zhang, G. Chen, K. Watanabe, and T. Taniguchi, Nano Lett. **17**(10), 6097–6103 (2017).
[9]J. Qin, G. Qiu, J. Jian, H. Zhou, L. Yang, A. Charnas, D. Y. Zemlyanov, C.-Y. Xu, X. Xu, and W. Wu, ACS Nano **11**(10), 10222–10229 (2017).
[10]J.-K. Qin, P.-Y. Liao, M. Si, S. Gao, G. Qiu, J. Jian, Q. Wang, S.-Q. Zhang, S. Huang, and A. Charnas, Nat. Electron. **3**(3), 141–147 (2020).
[11]L. Li, W. Han, L. Pi, P. Niu, J. Han, C. Wang, B. Su, H. Li, J. Xiong, and Y. Bando, InfoMat **1**(1), 54–73 (2019).
[12]K. Wu, E. Torun, H. Sahin, B. Chen, X. Fan, A. Pant, D. P. Wright, T. Aoki, F. M. Peeters, and E. Soignard, Nat. Commun. **7**(1), 12952 (2016).
[13]A. Khatibi, R. H. Godiksen, S. B. Basuvalingam, D. Pellegrino, A. A. Bol, B. Shokri, and A. G. Curto, 2D Mater. **7**(1), 015022 (2019).
[14]K. Wu, M. Blei, B. Chen, L. Liu, H. Cai, C. Brayfield, D. Wright, H. Zhuang, and S. Tongay, Adv. Mater. **32**(17), 2000018 (2020).
[15]J. A. Silva-Guillén, E. Canadell, P. Ordejón, F. Guinea, and R. Roldán, 2D Mater. **4**(2), 025085 (2017).
[16]S. Liu, W. Xiao, M. Zhong, L. Pan, X. Wang, H.-X. Deng, J. Liu, J. Li, and Z. Wei, Nanotechnology **29**(18), 184002 (2018).
[17]J. Dai and X. C. Zeng, Angew. Chem. **127**(26), 7682–7686 (2015).
[18]J. O. Island, M. Barawi, R. Biele, A. Almazán, J. M. Clamagirand, J. R. Ares, C. Sánchez, H. S. Van Der Zant, J. V. Álvarez, and R. D'Agosta, Adv. Mater. **27**(16), 2595–2601 (2015).
[19]J. O. Island, M. Buscema, M. Barawi, J. M. Clamagirand, J. R. Ares, C. Sánchez, I. J. Ferrer, G. A. Steele, H. S. van der Zant, and A. Castellanos-Gomez, Adv. Opt. Mater. **2**(7), 641–645 (2014).
[20]A. J. Molina-Mendoza, J. O. Island, W. S. Paz, J. M. Clamagirand, J. R. Ares, E. Flores, F. Leardini, C. Sánchez, N. Agraït, and G. Rubio-Bollinger, Adv. Funct. Mater. **27**(13), 1605647 (2017).
[21]A. Lipatov, P. M. Wilson, M. Shekhirev, J. D. Teeter, R. Netusil, and A. Sinitskii, Nanoscale **7**(29), 12291–12296 (2015).
[22]F. Saiz and R. Rurali, Nano Express **1**(1), 010026 (2020).
[23]R. Biele, E. Flores, J. R. Ares, C. Sanchez, I. J. Ferrer, G. Rubio-Bollinger, A. Castellanos-Gomez, and R. D'Agosta, Nano Res. **11**(1), 225–232 (2018).
[24]J. Silva-Guillén, E. Canadell, F. Guinea, and R. Roldán, ACS Photonics **5**(8), 3231–3237 (2018).
[25]W. Kong, C. Bacaksiz, B. Chen, K. Wu, M. Blei, X. Fan, Y. Shen, H. Sahin, D. Wright, and D. S. Narang, Nanoscale **9**(12), 4175–4182 (2017).
[26]C. Rice, R. Young, R. Zan, U. Bangert, D. Wolverson, T. Georgiou, R. Jalil, and K. Novoselov, Phys. Rev. B **87**(8), 081307 (2013).
[27]Y. Du, G. Qiu, Y. Wang, M. Si, X. Xu, W. Wu, and P. D. Ye, Nano Lett. **17**(6), 3965–3973 (2017).
[28]J.-K. Qin, C. Sui, Z. Qin, J. Wu, H. Guo, L. Zhen, C.-Y. Xu, Y. Chai, C. Wang, and X. He, Nano Lett. **21**(19), 8043–8050 (2021).
[29]X.-W. Fu, Z.-M. Liao, R. Liu, J. Xu, and D. Yu, ACS Nano **7**(10), 8891–8898 (2013).
[30]J. Greil, A. Lugstein, C. Zeiner, G. Strasser, and E. Bertagnolli, Nano Lett. **12**(12), 6230–6234 (2012).
[31]T. Mohiuddin, A. Lombardo, R. Nair, A. Bonetti, G. Savini, R. Jalil, N. Bonini, D. Basko, C. Galiotis, and N. Marzari, Phys. Rev. B **79**(20), 205433 (2009).
[32]Y. Wang, C. Cong, C. Qiu, and T. Yu, Small **9**(17), 2857–2861 (2013).
[33]M. Huang, H. Yan, C. Chen, D. Song, T. F. Heinz, and J. Hone, Proc. Natl. Acad. Sci. **106**(18), 7304–7308 (2009).
[34]Y. Wang, C. Cong, R. Fei, W. Yang, Y. Chen, B. Cao, L. Yang, and T. Yu, Nano Res. **8**(12), 3944–3953 (2015).
[35]S. Manzeli, A. Allain, A. Ghadimi, and A. Kis, Nano Lett. **15**(8), 5330–5335 (2015).